Journal of MATERIALS RESEARCH

Invited Paper
DOI:10.1557/s43578-024-01497-0

ANNUAL ISSUE

EARLY CAREER SCHOLARS IN MATERIALS SCIENCE, 2025

Dual-phase $Fe_{40}Mn_{20}Cr_{15}Ti_{10}Al_{10}Ni_5$ high-entropy alloy prepared by mechanical alloying and spark plasma sintering: Alloying behavior, thermal stability, and mechanical properties

Harsh Jain[1,a)], Yagnesh Shadangi[2], Lalit Kumar Singh[3], Ashutosh Kumar Dubey[1], Nilay Krishna Mukhopadhyay[3,a)]

[1] Department of Ceramic Engineering, Indian Institute of Technology (BHU) Varanasi, Varanasi, Uttar Pradesh 221005, India
[2] Department of Materials Science and Metallurgical Engineering, Indian Institute of Technology Bhilai, Durg, Chhattisgarh 491001, India
[3] Department of Metallurgical Engineering, Indian Institute of Technology (BHU) Varanasi, Varanasi, Uttar Pradesh 221005, India
[a)] Address all correspondence to these authors. e-mails: harshjain.rs.cer17@itbhu.ac.in; mukho.met@iitbhu.ac.in mukho_nk@rediffmail.com

Received: 27 June 2024; accepted: 25 November 2024; published online: 6 January 2025

The Fe-enriched high entropy alloy (HEA) shows the formation of BCC ($a = 0.287$ nm) and χ-phase ($a = 0.889$ nm) after mechanical alloying (MA) at 40 h. After spark plasma sintering (SPS) at 900 °C and 50 MPa, the dual-phase structure of FCC and BCC phases along with the χ-phase was observed. The average microhardness and elastic modulus of the SPSed sample were obtained as 5.6 ± 0.2 GPa and 131 ± 5 GPa respectively. The compressive yield strength of the SPSed sample was 1550 ± 100 MPa with ductility of ~ 11%. The dominant strengthening mechanisms are dislocation and grain boundary strengthening, which can account for ~ 65% of the observed flow stress. The correlation between the phases formed and thermal stability was correlated with different thermodynamic parameters and phase prediction by ThermoCalc software.

Harsh Jain

Harsh Jain currently works as a post-doctoral researcher in the Department of Metallurgical Engineering at the Indian Institute of Technology (BHU). He received his Bachelor of Technology in Mechanical Engineering from Shri Shankaracharya Institute of Engineering and Technology, Bhilai, India in 2012. He then completed his Master of Technology from the Department of Mechanical Engineering, National Institute of Technology Warangal, India in 2014. Subsequently, he was an Assistant Professor at MATS University Raipur, India from 2014 to 2017. Then he joined the Department of Ceramic Engineering, Indian Institute of Technology (BHU) Varanasi, India, completing his Ph.D. in 2023. Dr. Jain has presented his work at several national and international conferences in India and abroad. He got the International Travel Support Grant from SERB (DST) to attend the international conference in Jeju Island, South Korea. Dr. Jain is keenly interested in advanced materials processing, characterization, and mechanical and wear properties. He has published several research papers in reputed international journals on high entropy steel and ferrous alloys. He has extensively worked on high entropy metallic alloys and high entropy silicides. His work includes synthesis and materials processing through mechanical alloying, spark plasma sintering, and vacuum arc melting. He is interested in materials characterization through X-ray diffraction, electron microscopy, thermal analysis, instrumented indentation techniques, and properties like universal testing machines, universal tribometers, and in-vitro studies of metallic alloys.

Introduction

Conventional alloy systems were mostly focused on a single dominant element, which possesses low configurational entropy resulting in the formation of undesirable intermetallics [1]. However, high configurational entropy in the case of multi-principal element alloys (MPEAs) stabilized the single-phase random solid solution [1]. The high-entropy alloys mainly consisted of five or more principal elements mixed in equal or nearly equal proportions [1]. They have attracted the attention of the materials community due to their unique microstructure and excellent properties at high and cryogenic temperatures [2]. In recent years, several single-phase Face-Centered Cubic (FCC) [3], Body-Centered Cubic (BCC) [4], and Hexagonal Closed Packed (HCP) [5] HEAs were developed. FCC single-phase HEAs, particularly, Cantor alloy (CrCoFeMnNi) were studied extensively and these alloys have excellent room-temperature ductility and strength at cryogenic temperature [6]. But it lacks room-temperature strength. In contrast, single-phase BCC HEAs, i.e., NbMoTaW and VNbMoTaW refractory HEAs, showed good thermal stability and strength over the wide range of temperatures (873–1273 K) [4, 7]. However, BCC-structured HEAs have limited room-temperature tensile ductility.

Despite many advantages of single-phase HEAs, these alloys cannot meet the industrial requirements of strength and ductility. These issues have been addressed by the dual-phase or multiphase HEAs, which have a good combination of strength and ductility. In this context, lots of dual-phase HEAs were designed, including FeMnCoCr [8], $Fe_{49.85}Cr_{10.03}Mn_{10.03}Co_{10.03}Ni_{10.03}Al_{10.03}$ [9], $Fe_{36}Co_{21}Cr_{18}Ni_{15}Al_{10}$ [10], FeCoCrNiMnAl [11], $Al_{0.7}$CoCrFeNi [12], AlFeCoNiCu [13] and CrMnFeVTi [14] HEAs. These HEAs have been prepared using various synthesis routes and possess good strength. Further, they enhance the strength of dual-phase HEAs with the formation of nanoprecipitates (intermetallics) [15]. Some of the common nanoprecipitates (intermetallics) formed in HEAs are gamma prime (γ') [16], sigma (σ) [17], Laves [18], carbides [19], silicides [20] etc. These precipitates play a crucial role in enhancing the mechanical properties of the HEAs at room and high temperatures [21, 22].

However, dual-phase HEAs were mostly designed using costlier elements like Co and V, which increase the overall cost of the alloys and limit their commercialization. The work carried out in Co-free dual-phase HEAs, i.e., $Fe_{42}Ni_{12}Mn_{36}Al_8Ti_2$, $Fe_{36}Mn_{21}Cr_{18}Ni_{15}Al_{10}$ [23], $Fe_{28.2}Ni_{18.8}Mn_{32.9}Al_{14.1}Cr_6$, etc., have demonstrated good strength, but poor ductility and low fracture toughness. Generally, when the strength (tensile) is close to 1 GPa, these alloys become very brittle (ductility nearly ~ 1.1%) [23]. Therefore, the design of Co and V free Fe-enriched HEAs with good strength and ductility is highly desirable and worthy of further investigation.

Few high-entropy alloy systems consisting of Fe, Mn, Ni, Cr, Al, and Ti have been already reported, i.e., $(FeNi)_{67}Cr_{15}Mn_{10}Al_{8-x}Ti_x$ ($x = 3$, 4, and 5 at. %) [24], $Fe_{35}Mn_{20}Cr_{17}Ni_{12}Al_{12}Ti_4$ [10], $Fe_{37.06}Ni_{30.47}Mn_{12.44}Cr_{12.01}Al_{4.01}Ti_{4.01}$ [25], and $(Fe_{0.3}Ni_{0.3}Mn_{0.3}Cr_{0.1})_{88}Ti_4Al_8$ [15] HEAs, mostly focusing on the FCC/BCC phase and gamma prime as the secondary phase, and one along with some other precipitates. However, to stabilize the gamma prime phase in these alloys, the amount of Ni is minimum 10 at. % and this higher content of Ni unnecessarily increase the overall density of the alloys. These Fe-enriched HEAs normally prepared using the liquid phase route, which have certain drawbacks of segregation and evaporation of low melting point elements.[26, 27]. These drawbacks can be easily overcome by solid-state route, i.e., mechanical alloying followed by spark plasma sintering. The mechanical alloying forms the nanocrystalline and homogeneous alloys easily without chemical segregation [26]. The sintering of the nanostructured milled alloy powder samples were performed using the spark plasma sintering (SPS) which helps to retain the nanocrystallinity nature of the alloys, as it was sintered at a very high pulsed current [28–30].

A few researchers and co-workers discerned that the BCC/B2 phase has better strength in contrast to the FCC/γ' phase [10]. It was also observed that the nanoprecipitates formation in these alloys system further enhances the strength [21, 22]. Therefore, the present work envisages the design and development of Fe-enriched HEA having a trade-off between strength and ductility, comprising major FCC and minor BCC phases along with nano-precipitates. The addition of Ti and Al enhances the yield strength due to the formation of nanoprecipitate in Fe-enriched HEAs [10, 15, 24, 25]. The alloying addition of Mn and Cr was tuned for stabilizing the FCC and BCC phases. Further, a minor amount of Ni (~ 5 at. %) is added to stabilize the FCC phase. The alloying behavior and thermal stability of the as-milled Fe-enriched sample are analyzed. Further, for bulk samples, mechanical properties are evaluated using the microindentator and universal testing machine (UTM). Thermodynamic parameters are discussed to explain the phase formation after milling, annealing (at various temperatures) and SPS for the selected Fe-enriched HEAs. The calculation of Phase Diagrams (CALPHAD) data is correlated with experimentally observed phases.

Results

The melting temperature of the Fe-enriched HEA was estimated using the machine learning technique, the rule of mixture, and CALPHAD to be 1440 °C, 1455 °C and 1367 °C respectively. The formulae used to calculate the melting point through the machine learning approach [31], are as follows:

$$T_m = \frac{\sum_{i \neq j} T_{i-j} \times C_i \times C_j}{\sum_{i \neq j} C_i \times C_j}, \quad (1)$$

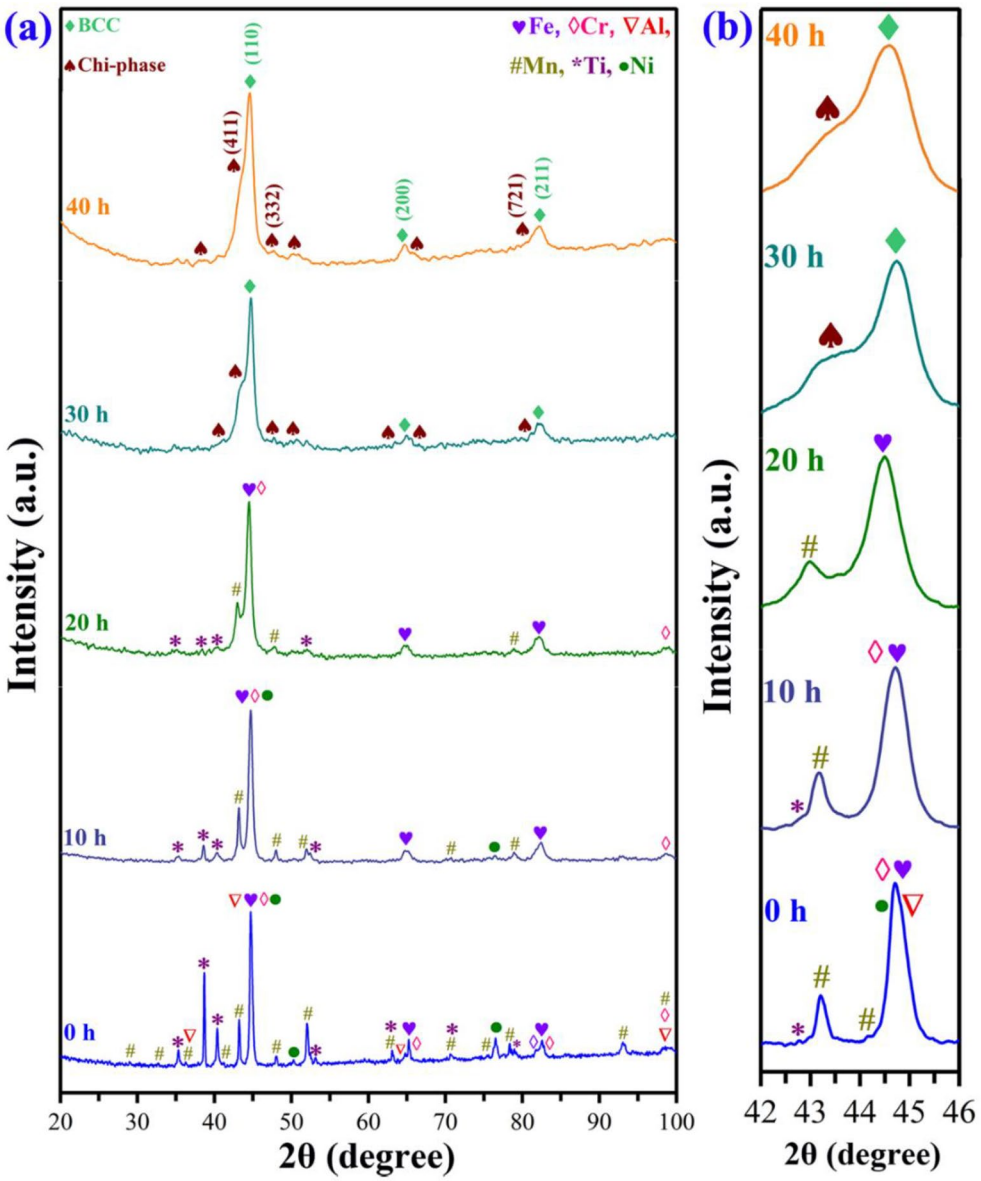

Figure 1: (a) XRD pattern of Fe-enriched HEA-milled powder sample at different milling times. (b) Blown-up image of the XRD pattern along the (110) plane in 2θ from 49° to 54°. This depicts the formation of BCC and χ-phase under 40 h of milling in the dual-phase HEA.

where T_{i-j} = binary liquidus temperature (°C); C_i and C_j = atomic percent of the i and j elements respectively. The value of the binary liquidus temperature is displayed in Supplementary Fig. 1. It was observed from the previous work on the HEAs that the melting point estimated through machine learning approach was closer to experimental findings as compared to that of the rule of mixture and CALPHAD approaches [32, 33].

XRD patterns of the pre-mixed (0 h), 10 h, 20 h, 30 h, and 40 h milled powder samples are [shown in Fig. 1(a)]. The diffraction peaks of the individual elements at the pre-mixed condition (0 h) are clearly shown in Fig. 1(a). As the milling time increases, the diffraction peak intensity decreases for all the elements, which are visible at different milling times [shown in Fig. 1(a)]. The low-intensity peaks and other peaks of Al vanished under 10 h, which was evident from Fig. 1(a). This happens because Al has the lowest melting temperature as compared to that of other elements present in the alloy system. As progressed to 20 h of milling, the peaks of Ni disappeared and after that Mn and Ti also vanished under 30 h of milling. The disappearance of Ni is due to low melting point and high diffusion coefficient as compared to that of other elements in the alloy system. The dual-phase structure of BCC (a = 0.287 nm; cI2) and χ-phase (a = 0.889 nm; cI52, close to gamma brass structure) was formed under 30 h of milling. The milling was

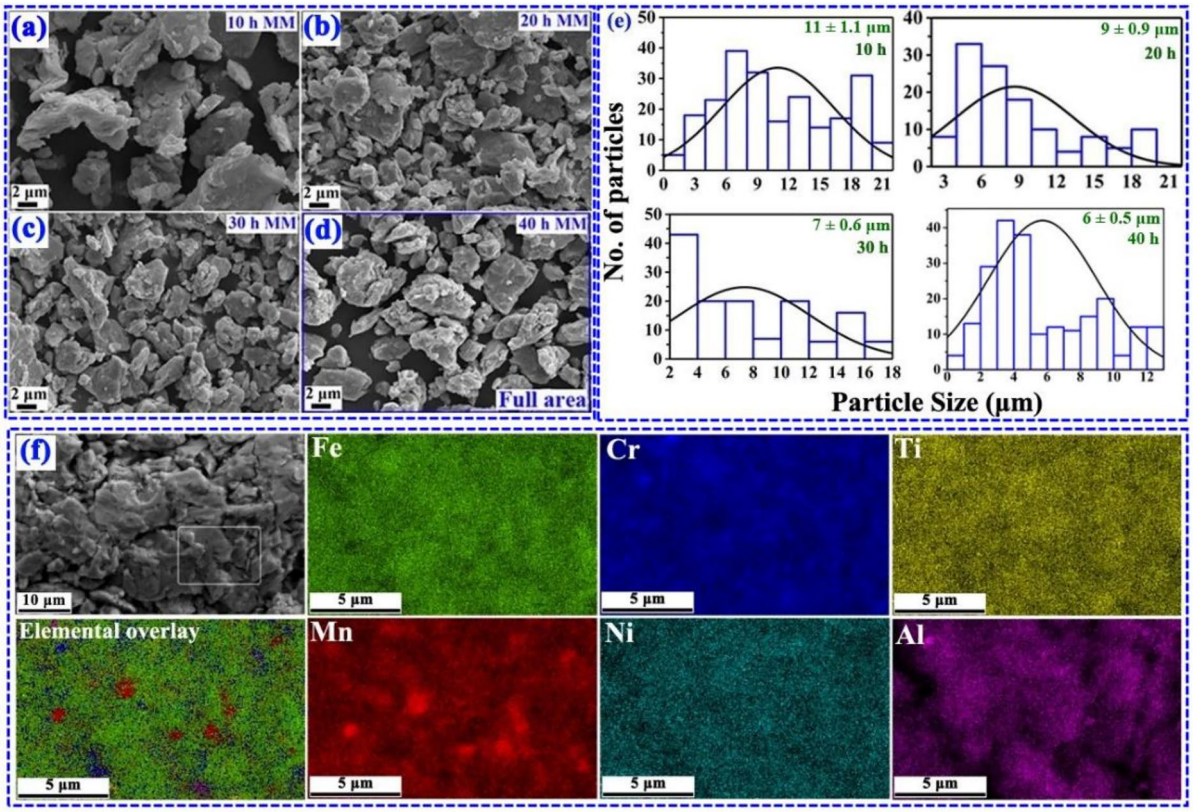

Figure 2: (a-d) SEM image (SE-mode) of the 10 h, 20 h, 30 h, and 40 h milled powder sample, respectively. (e) The histogram plot at 10 h, 20 h, 30 h, and 40 h of milling. (f) Area elemental mapping of the green compact pellet of 40 h milled sample. The histogram plot shows the varying particle size and mean particle size for 10 h, 20 h, 30 h, and 40 h milled powder samples, which were decreased with increased milling time. Area elemental mapping also confirmed the formation of a dual-phase structure of BCC and χ-phase, by showing two different contrast features , i.e., one is Fe rich (BCC) and another is Cr rich (χ-phase).

extended to 40 h to achieve a more homogeneous solid solution and refined grained microstructure. The BCC (as the major phase) and χ-phase (as the secondary phase) are identified after 40 h of milling. The enlarged view along the (110) plane from $2\theta = 42^{o}$ to 46^{o} has revealed the phase evolution with milling time [Fig. 1(b)].

The Rietveld refinement of the 40-h milled powder sample shown in Supplementary Fig. 2(a) also confirms the formation of BCC and χ-phase. Supplementary Fig. 2(b) shows the values of crystallite size (C.S.) and lattice strain (L.S.) at 30 h, 35 h, and 40 h of milling for the BCC phase and χ-phase. The goodness of fit (GoF) values were found to be 1.12, 1.17, and 1.10 and the reduced χ^2 values were found to be 1.23, 1.36, and 1.19 for the 30, 35, and 40 h milled samples respectively. The crystallite size decreases with the milling duration. The crystallite size for the BCC phase was refined from 21 ± 1.1 nm to 16 ± 0.7 nm as milling increases from 30 h to 40 h.

Similarly, the crystallite size for the χ-phase for 30 h and 40 h was found to be 24 ± 1.2 nm and 20 ± 1 nm, respectively. The lattice strain in the BCC phase increased from 1.56 ± 0.04 to 1.82 ± 0.011% for 30 h and 40 h milling, respectively. Similarly, the lattice strain of the χ-phase was increased from 1.02 ± 0.07 to 1.33 ± 0.03% as milling progressed from 30 h to 40 h. The reason for the increase in L.S. with milling time is due to the difference in atomic size and mechanical deformation of the powder particles. Lattice distortion occurs during milling, which brings extra grain refinement and lattice strain, affecting diffraction peak intensity and peak broadening. A slight increase in dislocation density was observed from 1.27×10^{18} m^{-2} to 1.92×10^{18} m^{-2} and 1.29×10^{18} m^{-2} to 2.02×10^{18} m^{-2} for BCC and χ-phase, respectively with milling. This type of trend in the dislocation density values with milling time was also observed in the MgAlSiCrFe [34], Al-IQC composite [30] and non-equiatomic high-entropy steel [35] prepared by mechanical alloying route. Supplementary Fig. 2(c and d) shows the values of structural parameters, phase fraction, and dislocation density in the Radar diagram for BCC and χ-phase respectively. A few other researchers and co-workers have used HR-XRD data for the Rietveld refinement of NiCoCrAlSi [36], TiZrHfTaNb [37], TiZrNbCrFe [38], $FeCoCrNi_2Al$ [39], non-equiatomic FeMnNiAlSiC [20] and FeMnNiTiAlSiC [19] high-entropy

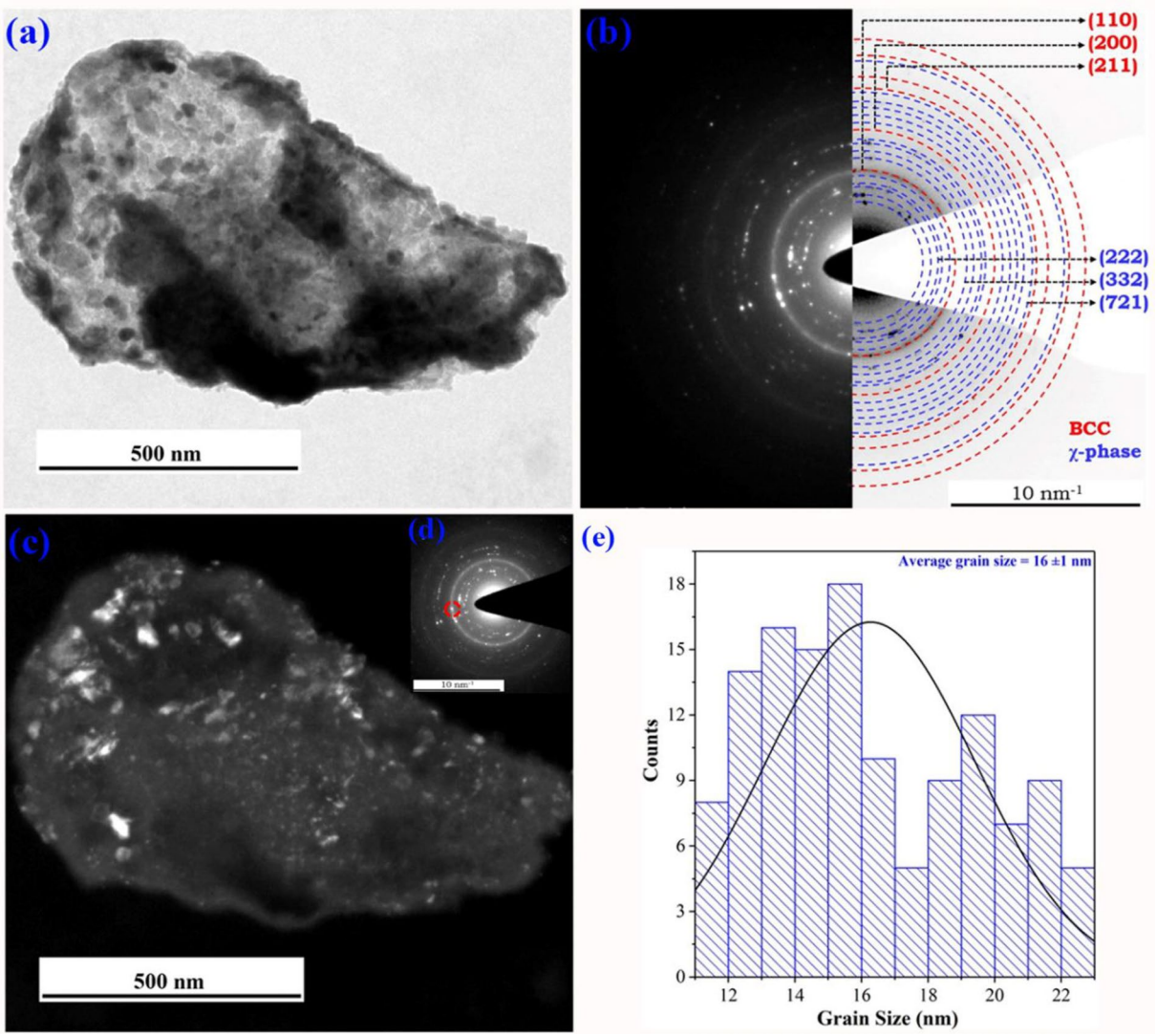

Figure 3: (a and b) TEM bright-field image of the 40-h milled powder sample and its corresponding SAD pattern, respectively. (c) Dark field image taken from the marked planes in insert (d). (e) Grain size distribution of the BCC phase.

alloys. The lattice constant, phase fraction, crystallite size and lattice strain were previously evaluated using the Rietveld refinement methods of similar quality of the HR-XRD data [19, 20, 36–39]. For the validity and robustness of the computed values i.e. lattice constant, crystallite size, and lattice strain using the Rietveld refinement method, the values were also calculated using the traditional approach i.e., W-H method and precision lattice measurement method, and listed in the Supplementary Table 1.

Figure 2(a–d) depicts the SEM image of the 10 h, 20 h, 30 h, and 40 h milled powder samples, which illustrate the powder particle size, shape, and morphology. The particle size at 10 h milled powder was varying from 1 to 22 μm and its average particle size was 11 ± 1.1 μm. The powder particles were randomly distributed and of different shapes, but as milling increased to 20 h, the average particle size was decreased to 9 ± 0.9 μm. Finally, in 40 h the average particle size was 6 ± 0.5 μm. Figure 2(e) shows the distribution of the particle size with milling time. The powder particle size and average particle size decreased with milling time. The powder particle has become more homogeneous as milling time progresses. The particle size was calculated using the absolute measurement methods in ImageJ software and the largest size was considered as particle size [40].

This type of particle size measurement calculation was previously done in low-density high-entropy alloys [28, 41] and composite [42]. Figure 2(d) also marks for the full-area EDS analysis of the as-milled powder sample. The values of the full-area EDS of the 40-h milled powder sample were listed in Supplementary Table 2, which depicts the presence of all the elements and

also shows the chemical homogeneity. Figure 2(f) illustrates the EDS area mapping of the 40 h green compact pellet of the Fe-enriched HEA. This shows that some region is enriched in Fe, corresponding to the BCC phase, and some area is enriched in Cr, related to χ-phase. The EDS area mapping also confirms the formation of a dual-phase structure consisting of BCC and χ-phase after 40 h of milling.

The bright-field image, corresponding selected area diffraction (SAD) pattern along with the dark field (DF) image are illustrated in Fig. 3(a–c) respectively. The dark patches evident on the bright field image [Fig. 3(a)] discern the high strain accumulation during the mechanical alloying leading to the formation of deformed grains. The polycrystalline nature of the SAD pattern indicates the random crystallographic texture and nanostructured Fe-enriched HEA milled sample. The careful investigation of the SAD pattern further confirmed the presence of BCC and χ-phase. The polycrystalline rings having d-spacings ~ 0.2026 n m, ~ 0.1433 nm, ~ 0.1170, ~ 0.1013 nm, ~ 0.0906, and ~ 0.0827 nm correspond to the presence of (110), (200), (211), (220), (310), and (222) reflections of BCC phase respectively. Further analysis shows the presence of (222), (332), and (721) reflections of the χ-phase. The DF image shows the formation of nanostructured grains corresponding to the (110) polycrystalline ring of BCC phase [Fig. 3(d)] arising from the extensive deformation by the repetitive fracturing and cold welding during mechanical alloying of Fe-enriched HEA [Fig. 3(c)]. The nanostructured grains of the milled powder were found to be ~ 16 ± 1 nm as shown in Fig. 3(e). The average grain size of the nanostructured grains of the BCC phase formed after 40 h of MA were in corroboration with the crystallite size of BCC phase as evident from Table 1.

The DSC curve of the 40-h powder sample is shown in Fig. 4(a). The curve displays the thermal stability of the as-milled alloy between 200 and 1000 °C. It has one exothermic event close to 540 °C (813 K), which is related to phase transformation. To correlate this phase transformation at 540 °C, the annealing of the 40 h powder sample was done at 400 °C, 500 °C, and 600 °C. XRD pattern at different temperatures is illustrated in Fig. 4(b).

The ex situ XRD reveals that the alloy is thermally stable up to 400 °C and afterward it forms the FCC solid solution around 540 °C. The annealed sample's lattice parameter, phase fraction, crystallite size and lattice strain at 400 °C, 500 °C, and 600 °C are calculated using the Rietveld refinement (Table 1). The Rietveld refinement analysis confirms the FCC solid solution phase formation at a higher temperature (600 °C). For comparison of the various annealed and milled samples with SPS, the XRD of the SPS sample is displayed in Fig. 4(b).

XRD pattern of the SPSed sample of the Fe-enriched HEA and its corresponding Rietveld refinement is shown in Fig. 5(a and b) respectively. The XRD analysis indicates the formation of dual-phase structure consisting of FCC (major) and BCC (secondary) along with χ-phase as nanoprecipitates. Rietveld refinement of the SPSed samples also confirmed the formation of a dual-phase structure along with precipitates. Its phase fraction, lattice parameter, crystallite size, and lattice strain are tabulated in Table 1. SEM (BSE mode) at different magnifications is illustrated in Fig. 6(a), showing the two types of contrast features as the light and dark gray region along with the dark gray-colored spherical precipitates. The light gray (1) contrast features are related to the BCC phase and the FCC phase is associated with dark gray contrast (2), as shown in Fig. 6(a). Figure 6(a) also represents spots corresponding to point-EDS and full-area EDS analysis and its values are listed in Supplementary Table 2. The full-area EDS analysis showed good chemical homogeneity in the SPSed Fe-enriched HEA. The point EDS analysis shows that point 1 is rich in Fe–Cr (related to BCC phase) and point 2 is rich in Fe–Mn–Ni, corresponding to the FCC phase. Elemental mapping depicts that the dark gray region is rich in Fe–Mn–Ni, corresponding to the FCC phase, and the light gray region is rich in Fe–Cr (BCC phase) [Fig. 6(b)].

To ascertain the fine structural and microstructural features of the SPSed sample, further analysis was carried

Table 1: The various phases formed at room temperature, annealed powder sample at 400 °C, 600 °C, and SPSed sample and its lattice parameter, phase fraction, crystallite size, and lattice strain.

Sample conditions	Phases formed	Lattice parameter (nm)	Phase fraction (%)	Crystallite size (nm)	Microstrain (%)
25 °C; GoF = 1.07, χ^2 = 1.11	BCC	0.2874 ± 0.0001	73.18	16 ± 0.7	1.82 ± 0.011
	χ-phase	0.8890 ± 0.0003	26.82	20 ± 1	1.33 ± 0.03
400 °C; GoF = 1.10, χ^2 = 1.18	BCC	0.2862 ± 0.0004	63.22	24 ± 1.2	0.66 ± 0.021
	χ-phase	0.8885 ± 0.0002	36.78	29 ± 1.8	0.74 ± 0.048
600 °C; GoF = 1.21, χ^2 = 1.35	BCC	0.2865 ± 0.0003	41.58	31 ± 1.5	0.54 ± 0.016
	FCC	0.3622 ± 0.0002	48.24	28 ± 1.1	0.49 ± 0.024
	χ-phase	0.8882 ± 0.0005	10.18	35 ± 2.2	0.65 ± 0.032
SPSed; GoF = 1.31, χ^2 = 1.52	BCC	0.2867 ± 0.0001	30.42	43 ± 2	0.25 ± 0.014
	FCC	0.3643 ± 0.0003	60.31	52 ± 1.8	0.30 ± 0.019
	χ-phase	0.8887 ± 0.0007	9.20	41 ± 3	0.22 ± 0.024

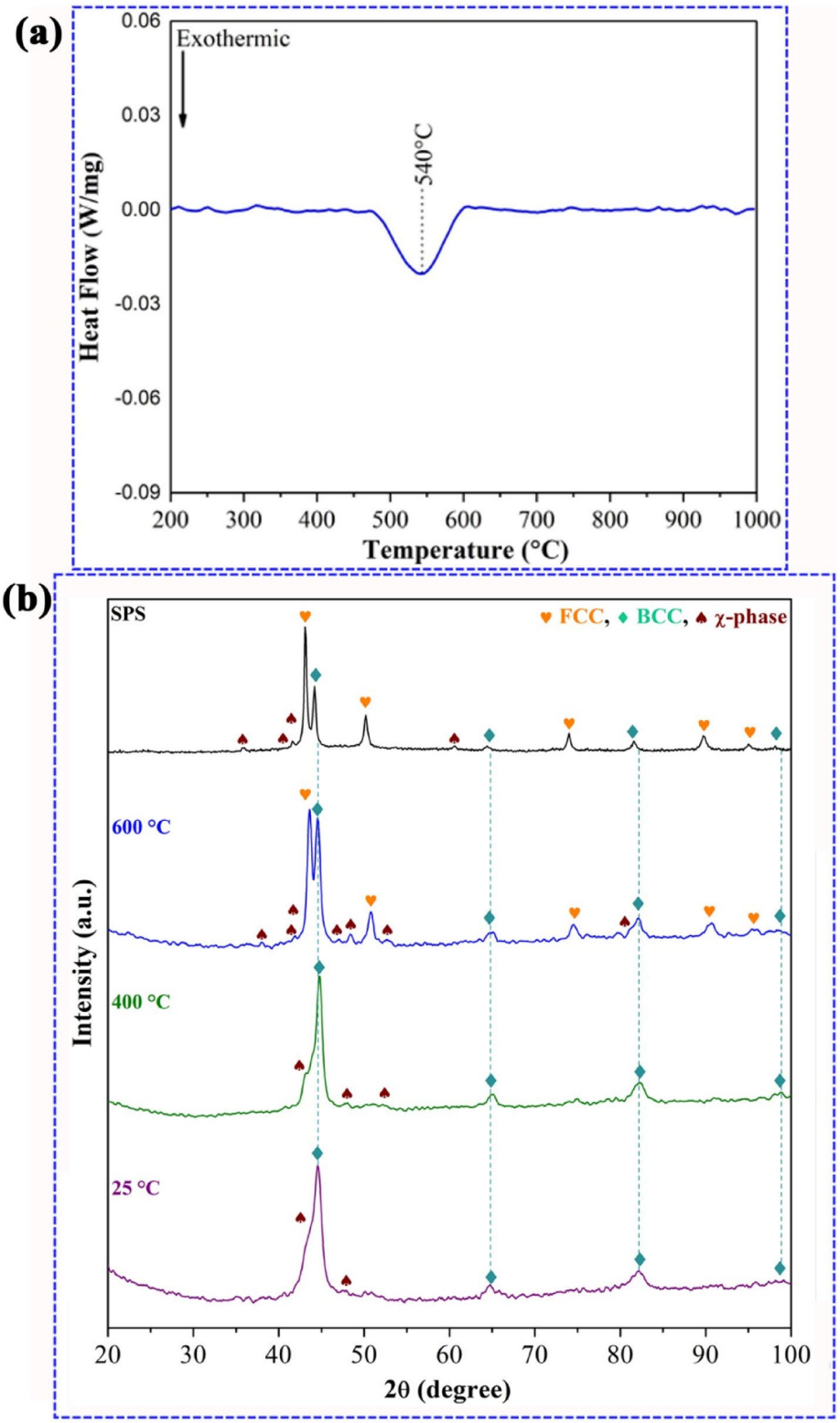

Figure 4: (a) DSC curve of the 40 h powder sample of dual-phase HEA. (b) XRD pattern of the 25 °C, 400 °C, 600 °C, and post-SPS. The curve exhibits exothermic events around 540 °C, which correlates with the FCC solid solution phase formation.

out using TEM, as shown in Fig. 7. Figure 7(a, b, and c) exhibits the bright-field TEM image of the SPSed sample where light (FCC), and dark (BCC) grains with nanoprecipitates can be observed. It can be discerned from the bright-field TEM image of the SPSed sample that the nanoprecipitates are formed inside the FCC and BCC matrix of the dual-phase Fe-enriched HEA, as shown in Fig. 7(a, b, and c). The selected area diffraction patterns illustrated in

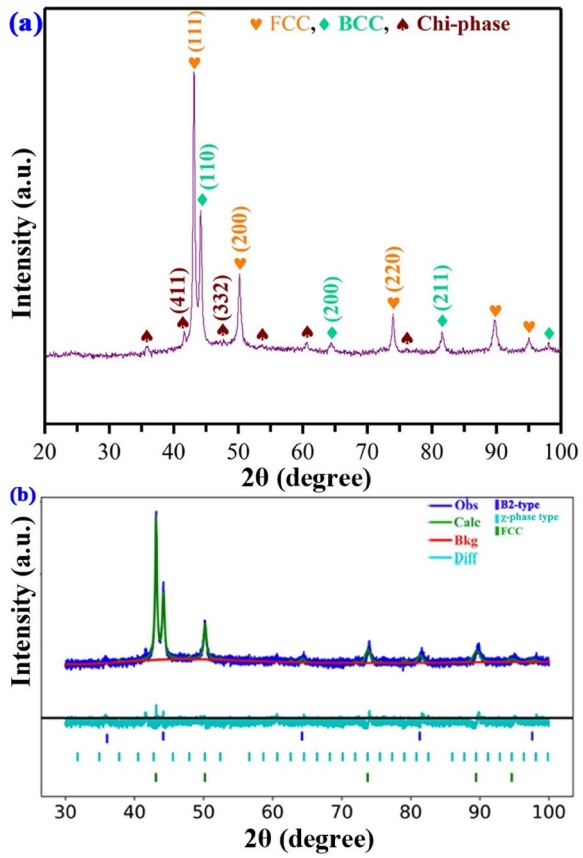

Figure 5: (a) XRD pattern of the SPSed sample of Fe-enriched HEA. (b) Its corresponding Rietveld refinement.

Fig. 7 (d, e, and f) confirm the formation of dual-phase i.e. FCC and BCC along with the χ-phase in the SPSed sample, which is in line with the XRDs. Further, the ring pattern displayed in Fig. 7(d and f) can be indexed as the plane for FCC as (111), (200), (220), and (311), and for χ-phase as (222), (220), (332), (411), (721), (800), and (660). The spot pattern represented in Fig. 7(e) indexed as BCC phase of (110), (200), and (310) planes with zone axis of [001] along with χ-phase spots were also seen and marked in brown circles. The dark field TEM image of the SPSed sample in Fig. 7(g and h) represents the presence of nanostructured grains (BCC) and nanoprecipitates (χ-phase) corresponding to the (110) plane of BCC and (411) plane and (332) plane of χ-phase. The nanostructured grains and nanoprecipitates in the SPSed samples are marked by white arrows in Fig. 7(g and h). This type of nanoprecipitate formation was also observed in the $(Fe_{0.3}Ni_{0.3}Mn_{0.3}Cr_{0.1})_{88}Ti_4Al_8$ HEA after the aging at 650 °C for 120 h [15]. The bright-field image shown in the Supplementary Fig. S3 (a, c, and d) depicts the presence of dislocation in the bulk SPSed sample. It was evident from the Supplementary Fig. 3 the presence of a dislocation wall (DW), dislocation forest (DF), and dislocation tangles (DT) in the SPSed sample. The SAD pattern (Supplementary Fig. 3(b)) was taken from Supplementary Fig. 3(a) which shows the reflections of FCC and χ-phase in the SPSed sample..

The indentation load vs depth of the indentation curve and its corresponding indentation spot of the SPSed sample are displayed in Fig. 8(a and b). The maximum load applied is 5000 mN and its corresponding depth of indentation is 6.4 μm in size. The optical image of the indentation mark does not reveal any crack formation up to 5000-mN load. The average hardness and elastic modulus of the SPSed sample are evaluated to be 5.7 ± 0.2 GPa and 131 ± 4 GPa respectively. Figure 8(c) illustrates the compressive stress vs strain curve at room temperature for the SPSed sample of Fe-enriched HEA. The values of ultimate and yield compressive strength were found to be 1900 ± 100 MPa and 1550 ± 100 MPa, respectively, with compressive ductility of 11%. The fractured surface (SEM image) after the compression test is shown in Fig. 8(d), exhibiting microvoids and cleavage. The fractured sample showed a dual kind of ductile and brittle fracture in dual-phase Fe-enriched HEA.

Discussion

Phase evolution and microstructure

The alloying behavior of dual-phase HEA was discussed during milling. At 10 h, the peaks of Al and low-intensity peaks were dissolved indicating the alloying process. The dissolving of Al also implies that it has the highest alloying rate, which can be attributed to the lowest melting temperature of Al. At 20 h, Cr and Ti disappeared. The disappearance of Ti was faster than Fe, this might be because Fe has a lower diffusion coefficient as compared to Ti. At 30 h, the Mn disappeared, and afterward dual-phase solid solution was formed having BCC (as the primary phase) and χ-phase (as the secondary phase). As Mn has the lowest diffusion coefficient among the other elements present in the alloy system. At 40 h, there is no phase change to be observed. The alloying behavior with milling time was pointed out in terms of the melting point and diffusion coefficient of individual elements in the HEA system [43]. They noticed that the elements having higher melting points and lower diffusion rates were dissolved slowly. The values of the physical and chemical properties of the elements present in the dual-phase HEA are mentioned in Supplementary Table 3. The BCC phase was formed after MA had the lattice parameter (a = 2.870 Å), which is close to α-Fe (acting as host lattice). The concept of host lattice after the milling of multicomponent alloys was advocated in AlCoCrFeMn HEA system [44]. The formation of χ-phase was also observed in the previously reported HEAs [19], $(Fe_{0.3}Ni_{0.3}Mn_{0.3}Cr_{0.1})_{88}Ti_4Al_8$ HEA [15], CoCrFeNi $(Ti_xAl_y)_{0.2}$ HEA [22], CoCrFeMnNi HEA [44], $Ti_{1.0}CrFe_2Ni_2$ [45] in the bulk samples.

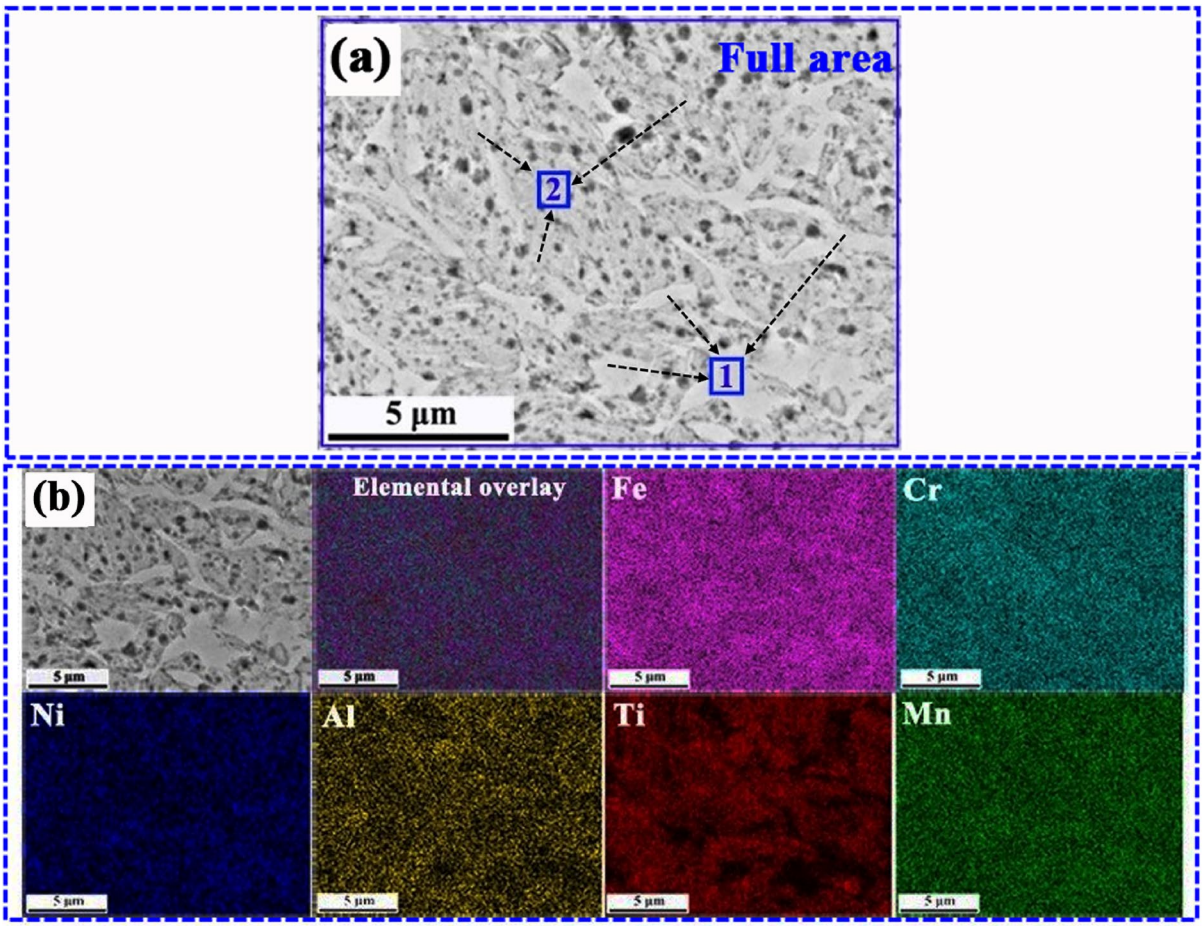

Figure 6: (a) SEM (BSE mode) of the SPSed sample. (b) Elemental mapping of the SPSed sample. This shows the two distinct features of light (BCC) and dark (FCC) gray.

The phase formation in dual-phase HEA after the MA and SPS was associated with the various thermodynamic parameters. The calculations of relevant thermodynamic parameters in the HEAs are mentioned in the previously reported HEAs [46, 47]. Zhang et al. [48] proposed the criteria to form the solid solutions in the HEAs system as: $-22 \le \Delta H_{mix} \le 7$, $11 \le \Delta S_{conf} \le 19.5$, and $\delta \le 6.6$. The values of the various thermodynamics parameters of the present system are listed in Supplementary Table 4, and it is well within the range of solid solution formation criteria. Guo et al. [49, 50] proposed the valence electron concentration parameter, which was used to predict the FCC/BCC/both, VEC ≥ 8.0 for FCC, VEC < 6.87 for BCC, 6.87 < VEC < 8.0 for BCC + FCC. In the present alloy system, it comes under the formation of the BCC phase. The milled alloyed powder formed the two BCC phase structures. However, the VEC parameter does not predict the number of phases and ordering/disordering in the structure of the HEAs [51]. After SPS, the alloy retained the BCC phase but formed the FCC solid solution. The formation of the FCC phase is due to binary enthalpy (~ 1 kJ/mol) between the Fe–Mn and the close atomic radius of Fe and Ni. The binary enthalpy of all the possible combinations is shown in Supplementary Fig. 4. The FCC phase was formed after the SPS was rich in Fe, Mn, and Ni, as listed in Table S1. The formation of the FCC phase in the $AlCrFeMnTi_5$ HEA system in arc-melted samples was also observed [52].

Thermal stability

For as-milled powder sample, thermal stability was investigated using the DSC analysis in the range of 200–1000 °C. Further, to substantiate the exothermic heating event at 540 °C, the ex situ XRD analysis of the annealed sample at 25, 400, and 600 °C was carried out. The as-milled powder sample showed thermal stability up to 400 °C; afterward, the evolution of FCC solid solution occurred at ~ 540 °C. The phases formed after the SPS were FCC and BCC along with χ-phase as nanoprecipitate. The

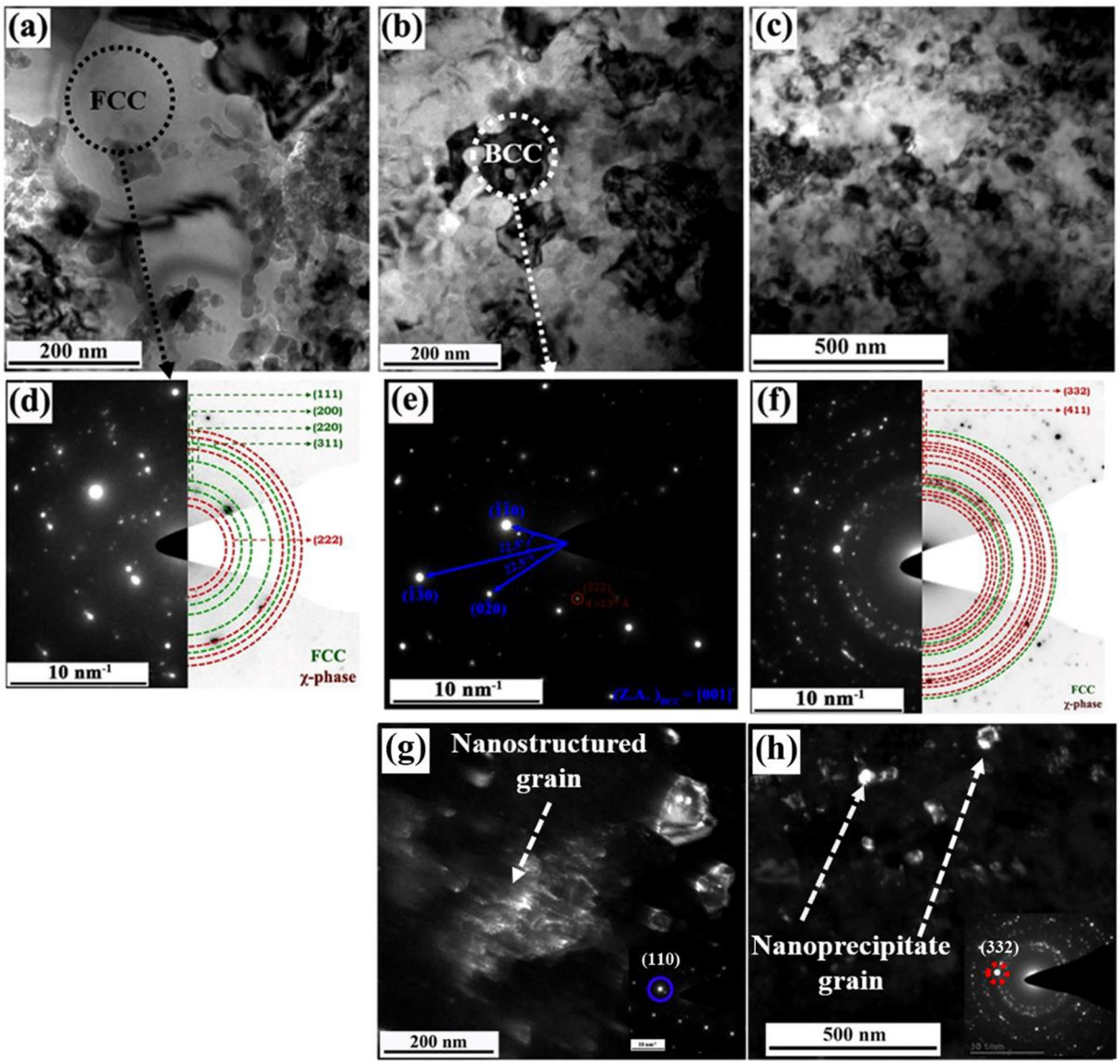

Figure 7: (a, b, and c) TEM bright-field image of the SPSed sample; (d, e, and f) its corresponding SAD pattern, respectively; (g and h) TEM dark field image of the SPSed sample. Bright-field images show the different contrast features dark gray and light gray corresponding to the BCC and FCC phase, respectively.

phase transformations occurred at higher temperatures due to metastable solid solution formation during milling. The χ-phase formation after the milling was dissolved at a higher temperature and transformed into a more stable FCC solid solution. The transformation of the χ-phase structure into a more stable phase was also observed in the duplex stainless steel and HEAs [53–55]. Generally, this type of χ-phase structure was observed in the Fe–Cr–Co and Fe–Cr–Mo steels, but this phase is metastable [53]. It was observed that Ti stabilizes the χ-phase in duplex stainless steel [54]. This type of dissolution of χ-phase (close to gamma brass) was also observed in previously reported HEAs, i.e., non-equiatomic FeMnNiTiAlSi-C HEAs [19]. The thermal stability of the HEA was correlated with the predicted phases from CALPHAD. The property diagram of the HEA is shown in Fig. 9(a). The various phase prediction from CALPHAD and their elemental stability with the temperature are displayed in Fig. 9(b-f). The predicted phases from the CALPHAD were BCC_A2 rich in Fe, Mn, and Cr, and FCC_A1 rich in Fe, Mn, and Ni as shown in Fig. 9(b and f). The BCC and FCC phase formation during the annealing and SPS process are well correlated with the predicted phases through the CALPHAD modeling. We observed a Fe–Cr-rich χ-phase in the experimental result, but this leading to inconsistency between the experimental result

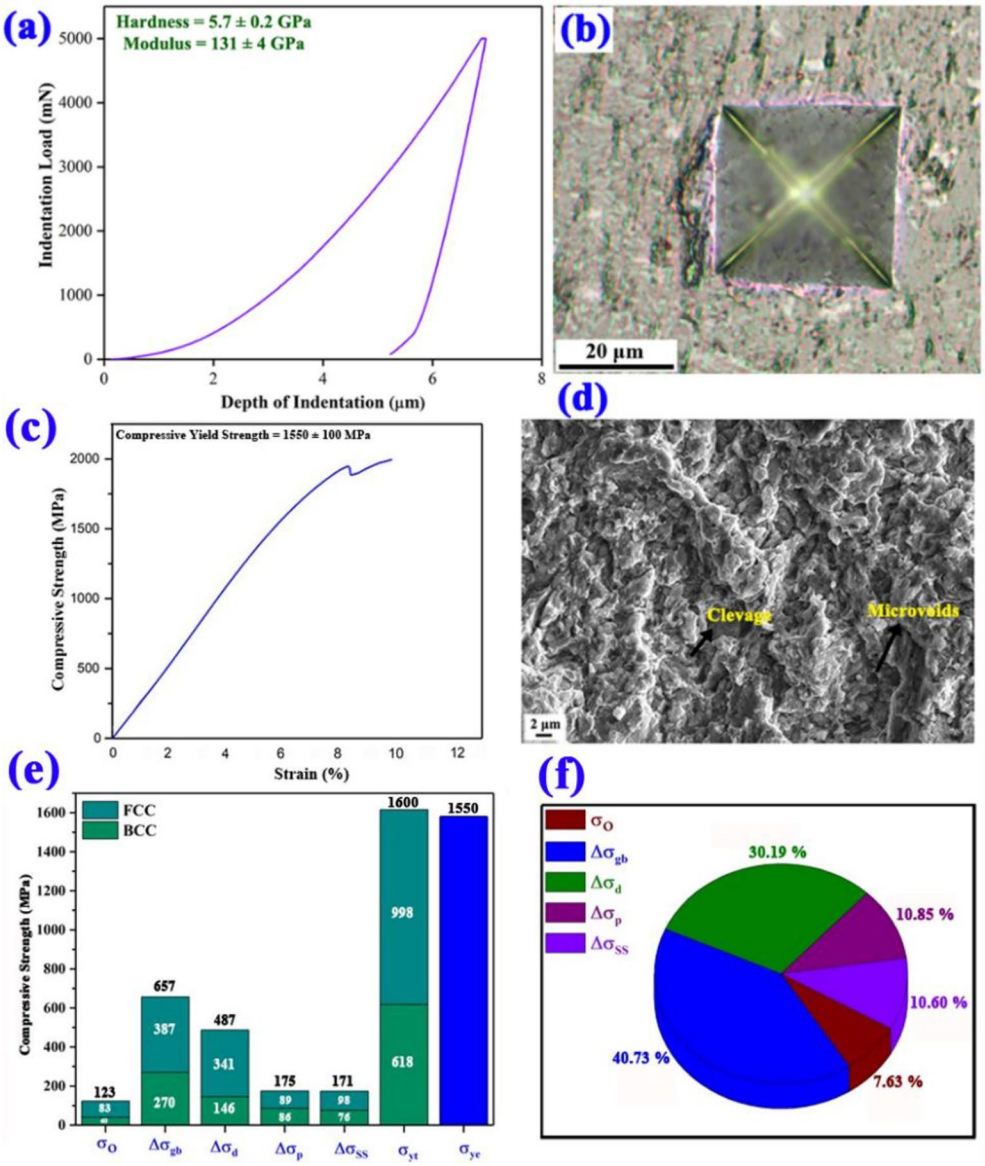

Figure 8: (a) Plot of indentation load vs depth of indentation. (b) Its corresponding image of indentation spot. (c) Compressive stress vs strain curve. (d) SEM of the fractured compressive sample. (e) Various theoretical strengthening mechanism and experimental yield strength values. (f) The percentages of the different strengthening mechanism and its contribution.

and model is due to a lack of the thermodynamic description of the χ-phase within the ThermoCalc database.

Mechanical properties and strengthening mechanisms

The dual-phase HEA shows a good yield compressive strength of 1550 MPa, which is 39.2% more than the single-phase Cantor alloy (1149 MPa) prepared using the powder metallurgy route [56]. It is observed that the strength in the metallic alloy systems is generally a combination of factors due to internal friction (σ_o), grain boundary ($\Delta\sigma_{gb}$), precipitates ($\Delta\sigma_p$), dislocation ($\Delta\sigma_d$), and solid solution ($\Delta\sigma_{ss}$) strengthening. Thus total strength of the dual-phase Fe-enriched HEA can be evaluated as follows:

$$\sigma_y = \sigma_o + \Delta\sigma_{gb} + \Delta\sigma_p + \Delta\sigma_d + \Delta\sigma_{ss}. \quad (2)$$

The frictional stress was 125 MPa and 120 MPa for FCC and BCC, respectively [56, 57]. The strengthening due to grain boundary was calculated using the Hall–Petch relation [19] as follows:

$$\Delta\sigma_{gb} = K_o d^{-1/2}, \quad (3)$$

where K_o = constant, taken as 494 MPa/μm$^{1/2}$ and 574 MPa/μm$^{1/2}$ for FCC and BCC, respectively [56, 58], and d is grain size. The average grain size was found to be 0.72 μm for FCC

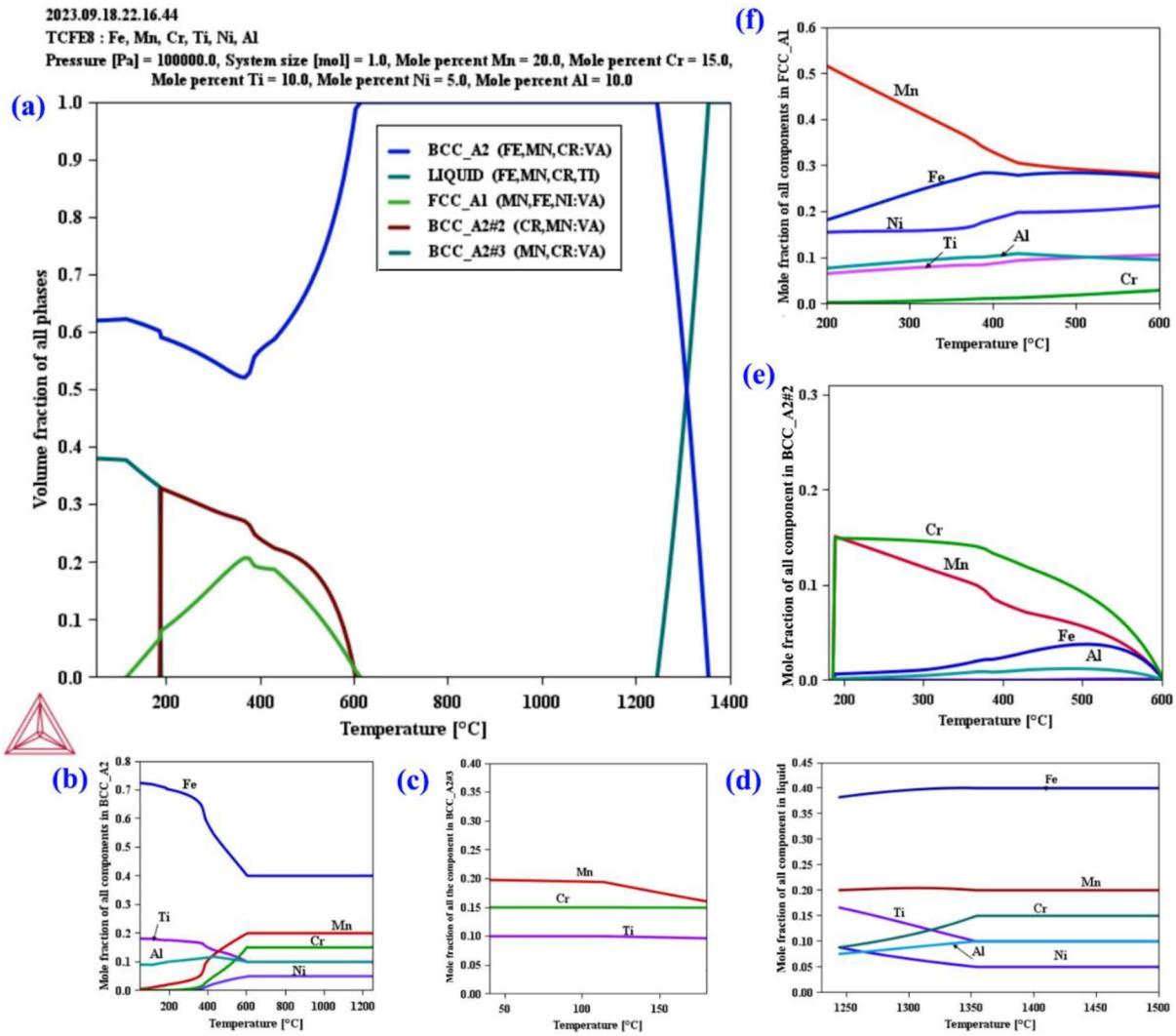

Figure 9: (a) Property diagram of Fe-enriched HEA. (b-f) Concentration (mol) of the various phase predicted and its elemental stability to temperature (TCFE8).

and 0.51 μm for BCC. The increment in strength due to the grain boundary is 582 MPa for FCC and 804 MPa for BCC.

The effect of the χ-phase nanoprecipitate in the FCC and BCC phases was estimated using the Orowan–Ashby equation [19]:

$$\Delta\sigma_{\mathrm{p}} = \frac{0.4M\mathrm{Gb}}{\pi\lambda}\frac{\ln\left(\frac{2\bar{r}}{b}\right)}{\sqrt{1-\upsilon}}, \tag{4}$$

where M = constant, and taken as 3.05 (FCC) and 2.73 (BCC), G = shear modulus, calculated from the rule of mixture and it is 77 GPa, υ = Poisson's ratio, and taken as 0.3, b = Burger vector, $(\frac{1}{\sqrt{2}}a)$ for FCC, and $(\frac{\sqrt{3}}{2}a)$ for BCC, where, a = lattice parameter, $\lambda = 2\bar{r}\left(\sqrt{\frac{\pi}{4f}} - 1\right)$ inter-precipitate space, f = 9.20% volume fraction of precipitate in the SPSed sample $\bar{r} = \sqrt{\frac{2}{3}}r$ and its value is 34.3 nm, and r = 82 nm precipitate's average radius. The strengthening values due to the χ-phase precipitate in the FCC and BCC phases are found to be 133 MPa and 257 MPa, respectively.

The increase in strength due to dislocation strengthening is calculated using the Bailey–Hirsch relationship [19]:

$$\Delta\sigma_{\mathrm{d}} = M\alpha Gb\sqrt{\rho_{\mathrm{dd}}}, \tag{5}$$

where α = constant and taken as 0.2 for FCC and BCC [57], b = Burger vector and ρ_{dd} = dislocation density [20, 42], and it is 1.78×10^{15} m^2 for FCC and 1.74×10^{15} m^2 for BCC. The strength due to dislocation strengthening was found to be 512 MPa for FCC and 435 MPa for BCC.

In HEAs, solid solution strengthening can be related to atomic radius among different atoms, and the strength due to this was estimated from the Fleischer model [19]:

$$\Delta\sigma_{\mathrm{ss}} = \frac{MG\varepsilon_{\mathrm{f}}}{700}c^{1/2}, \tag{6}$$

where c = concentration of the solute element in atomic percent and $\varepsilon_f = \left|\frac{\varepsilon_G}{1+0.5|\varepsilon_G|} - 3\varepsilon_a\right|^{3/2}$ is the relation parameter, $\varepsilon_G = \left(\frac{1}{G}\frac{dG}{dc}\right)$ is the modulus difference, and $\varepsilon_a = \left(\frac{1}{a}\frac{da}{dc}\right)$ is the atomic size misfit. Al and Ti were taken as solute elements for the BCC phase, and Mn for the FCC phase, these elements are of the highest atomic radius and their values are listed in Supplementary Table 2. The increase in yield strength due to solid solution was found to be 147 MPa for FCC and 226 MPa for BCC.

The contribution of the theoretical strengthening mechanisms considered in the present work is illustrated in Fig. 8(e). The percentage contribution of the FCC phase is 66.50% and the BCC phase is 33.50%. The strengthening due to grain boundary, precipitate, and dislocation are the dominant ones among the other strengthening mechanisms in the present alloy system. It was observed that the grain boundary strengthening was the primary strengthening mechanism in the HEAs prepared using the SPS [56]. This happens due to the fine-grained microstructure formation and its retention of the nanocrystalline nature after SPS [57]. Li et al. [56] showed that grain boundary strengthening is the dominant strengthening mechanism in CoCrFeMnNi HEA prepared using SPS. The present alloy system showed 39.20% greater strength to Cantor alloy [56], and this happened due to dislocation and precipitate strengthening. They are also the dominant strengthening mechanisms in the present alloy system, which together contribute ~ 40%. The contribution of all the strengthening mechanisms in percentage is displayed in Fig. 8(f). The calculated yield strength using the theoretical strengthening model is 1616 MPa, which is in reasonable agreement with the experimental compressive yield strength (1550 MPa). Therefore, it is possible to predict the strength of HEAs by theoretical strengthening mechanisms with certain approximations. A quantitative understanding of the relationship between microstructure and strength will provide a guideline for designing more advanced HEAs with desirable combinations of mechanical properties and superior performance in structural applications. It can be emphasized that the present alloy showed excellent compressive strength as compared to the other Fe-enriched HEAs [10, 15, 24, 25, 54], duplex steel [59], and low-density steel [60].

Conclusion

The following conclusions can be made from the present alloy system:

1. The Fe-enriched HEA was successfully prepared by MA, and it formed the dual-phase structure of BCC (a = 0.287 nm) and χ-phase structure (a = 0.889 nm) after 40 h of mechanical milling. This alloy showed the thermally stability up to 500 °C and transformed to the FCC phase around ~ 540 °C.
2. The SPSed sample retained the BCC phase (as secondary) and formed the FCC (a = 0.364 nm) as a major one along with χ-phase structure as nanoprecipitate (of ~ 16 nm size). The microhardness, elastic modulus, compressive yield strength and ductility were evaluated to be 5.7 ± 0.2 GPa, 131 ± 4 GPa, 1550 ± 100 MPa, and 11.0%, respectively.
3. The theoretical strengthening models were individually evaluated to find out the contribution toward experimental yield strength. The dominant strengthening mechanism is identified to be due to grain boundary and dislocation strengthening contributing to ~ 70% of the yield strength The contribution of precipitation strengthening mechanism is determined to be close to 10%.
4. The phase formation after MA and SPS matches well with the thermodynamic parameter's prediction. There is some inconsistency between the experimental phases and CALPHAD prediction, which may be due to the limitation of the database available (TCFE8).

Methodology

The high-energy ball mill (Fritsch Pulverisette 4) was used to prepare the Fe-enriched HEA using 43.34% Fe, 21.32% Mn, 15.13% Cr, 9.35% Ti, 5.69% Ni, and 5.27% Al (wt. %). The milling was done under the stainless steel vial and tungsten carbide (WC) ball at a speed of 200 rpm, and ball-to-powder ratio of 10:1. Toluene was used as the processing control agent to avert the contamination. The milling was stopped for 20 min in every 1 h of running to avoid overheating. To ascertain the alloying behavior with milling time, 3–4-g milled powder samples were taken out at intervals of 10 h. To consolidate the as-milled powder sample, the spark plasma sintering (SPS) (Model: FCT systems GmbH) was utilised for sintering at a temperature of 900 °C and 50 MPa pressure with 100 °C/min of heating rate and 15 min of holding time. The dimension achieved after the SPS was ~ 20 mm in diameter and ~ 10 mm in height. The samples were cut into the desired shape and size for further structural characterization and mechanical properties with the help of a wire EDM machine (Model: EXPRESSCUT EX-2530).

The thermal stability of the 40 h milled powder sample was analyzed using a differential scanning calorimeter (DSC) (Model: Netzsch, DSC404 Pegasus) in the temperature range of 200 °C to 1000 °C with a heating rate of 20 K/min under N_2 atmosphere. The structural analysis, i.e., X-Ray diffraction (XRD) after milling, and also after SPS was done using the X-Ray diffractometer ($\lambda_{k\alpha}$ = 1.542 Å) (Rigaku) operating at voltage and current of 40 kV and 15 mA. High-resolution XRD (Panalytical) ($\lambda_{k\alpha}$ = 1.783 Å) operating at the voltage

and current of 40 kV and 40 mA was also utilized. The scan rate was maintained at 5^0 min^{-1}. To correlate the DSC findings, a 40 h milled sample was annealed at different temperatures of 400 °C, 500 °C, and 600 °C with a holding time of 1 h and then water quenched. The sample for annealing was sealed in a quartz tube, which was backfilled with argon atmosphere. The quartz tubes carried the 40 h milled powder were separately heated at different temperatures (held for 1 h) and then water quenched. The ex situ XRD analysis of the annealed sample was done in the Rigaku X-Ray diffractometer.

The structural analysis of 40 h powder and SPSed was done using the transmission electron microscope (TEM) (TECNAI G^2T20), operating at 200 kV. The secondary electron (SE) imaging and the full-area chemical analysis by EDS of the milled powder samples were carried out using scanning electron microscopy (SEM) (Evo 18 Carl Zeiss), attached with the EDS detector. The mapping and point EDS analysis of the 40-h milled sample was performed by field emission scanning electron microscope (FESEM) (Nova Nano SEM 450) attached with EDS detector (1.37 eV Bruker). The microstructural features of SPSed sample and elemental analysis were done using the FESEM (Model: Nova Nano SEM 450), attached with an EDS detector. For microstructural features, the SPSed samples were systematically polished and chemically etched with the diluted Aquaregia solution. The sample was prepared for TEM analysis by electropolishing (twinjet electro polisher) using the solution of methanol (95 vol. %) and perchloric acid (5 vol. %) as etchant at the voltage of 20 V and 238 K (− 35 °C) temperature.

The structural parameters were determined using the XRD data of the powder, annealed, and SPSed samples with the help of the Rietveld refinement method in the general structural analysis system (GSAS-II) [61], Precision lattice parameter [27, 44], and Williamson-Hall method [35]. The Chebyshev-I background function with 10 coefficients was used to fit the background. The histogram scale factor was used to determine the phase fraction. To achieve the acceptable goodness of fit (GoF) the least square was adopted to minimize the difference between the experimental and observed data [62]. The other details of the refinement method were given elsewhere [19]. The calculation of dislocation density was described elsewhere [63].

The hardness measurement of the SPSed sample was done using the instrumented microhardness tester (Model: MHT^3, Anton Paar). The microhardness was measured at the applied load of 5000 mN and with the Vickers diamond indentator. The Oliver–Pharr method was used to calculate the hardness and elastic modulus [64]. The six measurements were made to calculate the average microhardness and elastic modulus of the SPSed samples. The compression test of the SPSed sample was performed using the 100-kN Instron Universal Testing Machine (Model: 5982). The sample dimension for the compression test was diameter (4 mm) to height (8 mm). The compressive strength was done at 25 °C with the crosshead speed of 0.5 mm/min. The microstructural features of the fractured sample after the compression test were examined using the SEM (Evo 18 Carl Zeiss).

Acknowledgments

The authors would like to thank Prof. R. K. Mandal and Dr. Rampada Manna for extending characterization facilities. The authors would also like to thank Prof. K G Prashanth for the spark plasma sintering facility. The support received from central Instrument Facility, IIT (BHU) is thankfully acknowledged. Authors would also like to acknowledge the DST-FIST project for infrastructural support (TPN-32537). YS would like to acknowledge the 'Research Initiation Grant' provided by IIT Bhilai.

Author contributions

Harsh Jain contributed to Conceptualization, Data curation, Investigation, Formal analysis, Methodology, and Writing-Original draft; Yagnesh Shadangi contributed to Conceptualization, Methodology, Investigation, Formal analysis, and Writing-Review and Editing; Lalit Kumar Singh contributed to Investigation and Data curation; Ashutosh Kumar Dubey contributed to Resources and Supervision; Nilay Krishna Mukhopadhyay contributed to Project administration, Supervision, Conceptualization, Resources, Formal analysis, and Writing-Review and Editing.

Funding

No funding was received for conducting this study.

Data availability

Data will be made available on reasonable request.

Declarations

Competing interest On behalf of all authors, the corresponding author states that there is no conflict of interest.

Supplementary Information

The online version contains supplementary material available at https://doi.org/10.1557/s43578-024-01497-0.

References

1. B.S. Murty, J.-W. Yeh, S. Ranganathan, P.P. Bhattacharjee, *High-Entropy Alloys* (Elsevier, New York, 2019). https://doi.org/10.1016/b978-0-12-816067-1.09987-2
2. D.B. Miracle, O.N. Senkov, A critical review of high entropy alloys and related concepts. Acta Mater. **122**, 448–511 (2017). https://doi.org/10.1016/j.actamat.2016.08.081
3. B. Cantor, I.T.H. Chang, P. Knight, A.J.B. Vincent, Microstructural development in equiatomic multicomponent alloys. Mater. Sci. Eng. A **375–377**, 213–218 (2004). https://doi.org/10.1016/j.msea.2003.10.257
4. O.N. Senkov, G.B. Wilks, D.B. Miracle, C.P. Chuang, P.K. Liaw, Refractory high-entropy alloys. Intermetallics **18**, 1758–1765 (2010). https://doi.org/10.1016/j.intermet.2010.05.014
5. Y.J. Zhao, J.W. Qiao, S.G. Ma, M.C. Gao, H.J. Yang, M.W. Chen, Y. Zhang, A hexagonal close-packed high-entropy alloy: the effect of entropy. Mater. Des. **96**, 10–15 (2016). https://doi.org/10.1016/j.matdes.2016.01.149
6. B. Cantor, Multicomponent high-entropy Cantor alloys. Prog. Mater. Sci. (2021). https://doi.org/10.1016/j.pmatsci.2020.100754
7. O.N. Senkov, G.B. Wilks, J.M. Scott, D.B. Miracle, Mechanical properties of $Nb_{25}Mo_{25}Ta_{25}W_{25}$ and $V_{20}Nb_{20}Mo_{20}Ta_{20}W_{20}$ refractory high entropy alloys. Intermetallics **19**, 698–706 (2011). https://doi.org/10.1016/j.intermet.2011.01.004
8. Z. Li, C.C. Tasan, K.G. Pradeep, D. Raabe, A TRIP-assisted dual-phase high-entropy alloy: grain size and phase fraction effects on deformation behaviour. Acta Mater. **131**, 323–335 (2017). https://doi.org/10.1016/j.actamat.2017.03.069
9. C. Chen, W. Zhang, E. Zhang, W. Wang, R. Wei, J. Chen, S. Yuan, T. Wang, T. Zhang, S. Guan, J. Jiang, F. Li, Microstructure of and mechanical properties of an as-cast fine-grain dual-phase Fe-based high entropy alloy formed via solid-state phase transformation. Mater. Sci. Eng. A (2022). https://doi.org/10.1016/j.msea.2022.142779
10. N.D. Stepanov, D.G. Shaysultanov, M.A. Tikhonovsky, S.V. Zherebtsov, Structure and high temperature mechanical properties of novel non-equiatomic Fe-(Co, Mn)-Cr-Ni-Al-(Ti) high entropy alloys. Intermetallics **102**, 140–151 (2018). https://doi.org/10.1016/j.intermet.2018.09.010
11. Y. Cui, J. Shen, S.M. Manladan, K. Geng, S. Hu, Strengthening mechanism in two-phase FeCoCrNiMnAl high entropy alloy coating. Appl. Surf. Sci. (2020). https://doi.org/10.1016/j.apsusc.2020.147205
12. K. Srimark, S. Dasari, A. Sharma, P. Wangyao, B. Gwalani, T. Rojhirunsakool, S. Gorsse, R. Banerjee, Hierarchical phase evolution in a lamellar $Al_{0.7}$CoCrFeNi high entropy alloy involving competing metastable and stable phases. Scr. Mater. (2021). https://doi.org/10.1016/j.scriptamat.2021.114137
13. M.B. Kivy, M.A. Zaeem, S. Lekakh, Investigating phase formations in cast AlFeCoNiCu high entropy alloys by combination of computational modeling and experiments. Mater. Des. **127**, 224–232 (2017). https://doi.org/10.1016/j.matdes.2017.04.086
14. R.K. Song, L.J. Wei, C.X. Yang, S.J. Wu, Phase formation and strengthening mechanisms in a dual-phase nanocrystalline CrMnFeVTi high-entropy alloy with ultrahigh hardness. J. Alloys Compd. **744**, 552–560 (2018). https://doi.org/10.1016/j.jallcom.2018.02.029
15. M. Luebbe, J. Duan, F. Zhang, J. Poplawsky, H. Pommeranke, M. Arivu, A. Hoffman, M. Buchely, H. Wen, A high-strength precipitation hardened cobalt-free high-entropy alloy. Mater. Sci. Eng. A (2023). https://doi.org/10.1016/j.msea.2023.144848
16. B. Han, J. Wei, Y. Tong, D. Chen, Y. Zhao, J. Wang, F. He, T. Yang, C. Zhao, Y. Shimizu, K. Inoue, Y. Nagai, A. Hu, C.T. Liu, J.J. Kai, Composition evolution of gamma prime nanoparticles in the Ti-doped CoFeCrNi high entropy alloy. Scr. Mater. **148**, 42–46 (2018). https://doi.org/10.1016/j.scriptamat.2018.01.025
17. M.H. Tsai, K.Y. Tsai, C.W. Tsai, C. Lee, C.C. Juan, J.W. Yeh, Criterion for sigma phase formation in Cr- and V-Containing high-entropy alloys. Mater. Res. Lett. **1**, 207–212 (2013). https://doi.org/10.1080/21663831.2013.831382
18. T. Li, H. Chen, Z. Zhou, S. Li, Y.D. Wang, Enhanced strength and ductility by a core-shell-like distributed Laves phase in $Cr_{15}Ti_{25}Zr_{25}Hf_{25}Sc_{10}$ high-entropy alloy. Intermetallics (Barking) (2023). https://doi.org/10.1016/j.intermet.2022.107753
19. H. Jain, Y. Shadangi, D. Chakravarty, A.K. Dubey, N.K. Mukhopadhyay, High entropy steel processed through mechanical alloying and spark plasma sintering: alloying behaviour, thermal stability and mechanical properties. Mater. Sci. Eng. A (2022). https://doi.org/10.1016/j.msea.2022.144029
20. H. Jain, Y. Shadangi, D. Chakravarty, K. Chattopadhyay, A.K. Dubey, N.K. Mukhopadhyay, Low-density $Fe_{40}Mn_{19}Ni_{15}Al_{15}Si_{10}C_1$ high entropy steel processed by

mechanical alloying and spark plasma sintering: phase evolution, microstructure and mechanical properties. Mater. Sci. Eng. A (2023). https://doi.org/10.1016/j.msea.2023.144776.

21. I. Basu, J.T.M. De Hosson, Strengthening mechanisms in high entropy alloys: fundamental issues. Scr. Mater. **187**, 148–156 (2020). https://doi.org/10.1016/j.scriptamat.2020.06.019
22. J.Y. He, H. Wang, H.L. Huang, X.D. Xu, M.W. Chen, Y. Wu, X.J. Liu, T.G. Nieh, K. An, Z.P. Lu, A precipitation-hardened high-entropy alloy with outstanding tensile properties. Acta Mater. **102**, 187–196 (2016). https://doi.org/10.1016/j.actamat.2015.08.076
23. D.G. Shaysultanov, G.A. Salishchev, Y.V. Ivanisenko, S.V. Zherebtsov, M.A. Tikhonovsky, N.D. Stepanov, Novel $Fe_{36}Mn_{21}Cr_{18}Ni_{15}Al_{10}$ high entropy alloy with bcc/B2 dual-phase structure. J. Alloys Compd. **705**, 756–763 (2017). https://doi.org/10.1016/j.jallcom.2017.02.211
24. Y.L. Zhao, T. Yang, J.H. Zhu, D. Chen, Y. Yang, A. Hu, C.T. Liu, J.J. Kai, Development of high-strength Co-free high-entropy alloys hardened by nanosized precipitates. Scr. Mater. **148**, 51–55 (2018). https://doi.org/10.1016/j.scriptamat.2018.01.028
25. R. Mohammadzadeh, A. Heidarzadeh, H.T. Serindağ, G. Çam, Microstructure and mechanical response of novel Co-free FeNiMnCrAlTi high-entropy alloys. J. Mater. Res. Technol. **26**, 2043–2049 (2023). https://doi.org/10.1016/j.jmrt.2023.08.039
26. M. Vaidya, G.M. Muralikrishna, B.S. Murty, High-entropy alloys by mechanical alloying: a review. J. Mater. Res. **34**, 664–686 (2019). https://doi.org/10.1557/jmr.2019.37
27. P. Pradhan, Y. Shadangi, V. Shivam, N.K. Mukhopadhyay, Powder metallurgical processing of CrMnFeCoMo high entropy alloy: phase evolution, microstructure, thermal stability and mechanical properties. J. Alloys Compd. (2023). https://doi.org/10.1016/j.jallcom.2022.168002
28. N. Singh, Y. Shadangi, V. Shivam, N.K. Mukhopadhyay, MgAlSiCrFeNi low-density high entropy alloy processed by mechanical alloying and spark plasma sintering: effect on phase evolution and thermal stability. J. Alloys Compd. (2021). https://doi.org/10.1016/j.jallcom.2021.159923
29. S. Praveen, B.S. Murty, R.S. Kottada, Phase evolution and densification behavior of nanocrystalline multicomponent high entropy alloys during spark plasma sintering. JOM **65**, 1797–1804 (2013). https://doi.org/10.1007/s11837-013-0759-0
30. Y. Shadangi, S. Sharma, V. Shivam, J. Basu, K. Chattopadhyay, B. Majumdar, N.K. Mukhopadhyay, Fabrication of Al–Cu–Fe quasicrystal reinforced 6082 aluminium matrix nanocomposites through mechanical milling and spark plasma sintering. J. Alloys Compd. (2020). https://doi.org/10.1016/j.jallcom.2020.154258
31. J. Qi, A.M. Cheung, S.J. Poon, High entropy alloys mined from binary phase diagrams. Sci. Rep. (2019). https://doi.org/10.1038/s41598-019-50015-4
32. H. Yanxon, J. Weng, H. Parraga, W. Xu, U. Ruett, N. Schwarz, Artifact identification in X-ray diffraction data using machine learning methods. J. Synchrotron Radiat. **30**(1), 137–146 (2022)
33. B. Debnath, A. Vinoth, M. Mukherjee, S. Datta, Designing Fe-based high entropy alloy—a machine learning approach. IOP Conf. Ser. Mater. Sci. Eng. (2020). https://doi.org/10.1088/1757-899X/912/5/052021
34. N. Singh, Y. Shadangi, G.S. Goud, V.K. Pandey, V. Shivam, N.K. Mukhopadhyay, Fabrication of MgAlSiCrFe low-density high-entropy alloy by mechanical alloying and spark plasma sintering. Trans. Indian Inst. Metals. (2021). https://doi.org/10.1007/s12666
35. H. Jain, Y. Shadangi, V. Shivam, D. Chakravarty, N.K. Mukhopadhyay, D. Kumar, Phase evolution and mechanical properties of non-equiatomic Fe–Mn–Ni–Cr–Al–Si–C high entropy steel. J. Alloys Compd. (2020). https://doi.org/10.1016/j.jallcom.2020.155013
36. A. Shahbazkhan, H. Sabet, M. Abbasi, Microstructural and mechanical properties of NiCoCrAlSi high entropy alloy fabricated by mechanical alloying and spark plasma sintering. J. Alloys Compd. (2022). https://doi.org/10.1016/j.jallcom.2021.163041
37. C. Zlotea, M.A. Sow, G. Ek, J.P. Couzinié, L. Perrière, I. Guillot, J. Bourgon, K.T. Møller, T.R. Jensen, E. Akiba, M. Sahlberg, Hydrogen sorption in TiZrNbHfTa high entropy alloy. J. Alloys Compd. **775**, 667–674 (2019). https://doi.org/10.1016/j.jallcom.2018.10.108
38. R. Floriano, G. Zepon, K. Edalati, G.L.B.G. Fontana, A. Mohammadi, Z. Ma, H.W. Li, R.J. Contieri, Hydrogen storage properties of new A3B2-type TiZrNbCrFe high-entropy alloy. Int. J. Hydrogen Energy **46**, 23757–23766 (2021). https://doi.org/10.1016/j.ijhydene.2021.04.181
39. M.S. Jadhav, D. Sahane, A. Verma, S. Singh, Thermal stability and thermal expansion behavior of $FeCoCrNi_2Al$ high entropy alloy. Adv. Powder Technol. **32**, 378–384 (2021). https://doi.org/10.1016/j.apt.2020.12.019
40. V. Shivam, J. Basu, Y. Shadangi, M.K. Singh, N.K. Mukhopadhyay, Mechano-chemical synthesis, thermal stability and phase evolution in AlCoCrFeNiMn high entropy alloy. J. Alloys Compd. **757**, 87–97 (2018). https://doi.org/10.1016/j.jallcom.2018.05.057
41. V.K. Pandey, Y. Shadangi, V. Shivam, J. Basu, K. Chattopadhyay, B. Majumdar, B.N. Sarma, N.K. Mukhopadhyay, Synthesis, characterization and thermal stability of nanocrystalline MgAlMnFeCu low-density high-entropy alloy. Trans. Indian Inst. Met. **74**, 33–44 (2021). https://doi.org/10.1007/s12666-020-02114-4
42. Y. Shadangi, K. Chattopadhyay, N.K. Mukhopadhyay, Powder metallurgical processing of Al matrix composite reinforced with AlSiCrMnFeNiCu high-entropy alloys: microstructure,

thermal stability, and microhardness. J. Mater. Res. (2023). https://doi.org/10.1557/s43578-022-00866-x
43. V. Shivam, J. Basu, V.K. Pandey, Y. Shadangi, N.K. Mukhopadhyay, Alloying behaviour, thermal stability and phase evolution in quinary AlCoCrFeNi high entropy alloy. Adv. Powder Technol. **29**, 2221–2230 (2018). https://doi.org/10.1016/j.apt.2018.06.006
44. L.Z. Medina, L. Riekehr, U. Jansson, Phase formation in magnetron sputtered CrMnFeCoNi high entropy alloy. Surf. Coat. Technol. (2020). https://doi.org/10.1016/j.surfcoat.2020.126323
45. G.J. Diao, A.Q. He, Y.Q. Tang, M.Y. Wu, D. Zhang, W.G. Chen, D.L. Chen, D.Y. Li, Effects of Al and Ti on microstructure, mechanical properties and wear resistance of $Ti_XCrFe_2Ni_2$ alloys. Mater. Sci. Eng. A (2023). https://doi.org/10.1016/j.msea.2023.145242
46. X. Yang, Y. Zhang, Prediction of high-entropy stabilized solid-solution in multi-component alloys. Mater. Chem. Phys. **132**, 233–238 (2012). https://doi.org/10.1016/j.matchemphys.2011.11.021
47. A.R. Miedema, P.F. de Châtel, F.R. de Boer, Cohesion in alloys—fundamentals of a semi-empirical model. Physica B+C **100**, 1–28 (1980). https://doi.org/10.1016/0378-4363(80)90054-6
48. Y. Zhang, Y.J. Zhou, J.P. Lin, G.L. Chen, P.K. Liaw, Solid-solution phase formation rules for multi-component alloys. Adv. Eng. Mater. **10**, 534–538 (2008). https://doi.org/10.1002/adem.200700240
49. S. Guo, Phase selection rules for cast high entropy alloys: an overview. Mater. Sci. Technol. **31**, 1223–1230 (2015). https://doi.org/10.1179/1743284715y.0000000018
50. S. Guo, C.T. Liu, Phase stability in high entropy alloys: formation of solid-solution phase or amorphous phase. Progr. Nat. Sci. **21**, 433–446 (2011). https://doi.org/10.1016/S1002-0071(12)60080-X
51. N.D. Stepanov, D.G. Shaysultanov, G.A. Salishchev, M.A. Tikhonovsky, E.E. Oleynik, A.S. Tortika, O.N. Senkov, Effect of v content on microstructure and mechanical properties of the CoCrFeMnNiV_x high entropy alloys. J. Alloys Compd. **628**, 170–185 (2015). https://doi.org/10.1016/j.jallcom.2014.12.157
52. S. Wu, Y. Pan, J. Lu, N. Wang, W. Dai, T. Lu, Effect of the addition of Mg Ti, Ni on the decoloration performance of AlCrFeMn high entropy alloy. J. Mater. Sci. Technol. **35**, 1629–1635 (2019). https://doi.org/10.1016/j.jmst.2019.03.025
53. A.D. Warren, R.L. Harniman, Z. Guo, C.M. Younes, P.E.J. Flewitt, T.B. Scott, Quantification of sigma-phase evolution in thermally aged 2205 duplex stainless steel. J. Mater. Sci. **51**, 694–707 (2016). https://doi.org/10.1007/s10853-015-9131-9
54. D.M. Escriba, E. Materna-Morris, R.L. Plaut, A.F. Padilha, Chi-phase precipitation in a duplex stainless steel. Mater Charact **60**, 1214–1219 (2009). https://doi.org/10.1016/j.matchar.2009.04.013
55. B. Gwalani, A.V. Ayyagari, D. Choudhuri, T. Scharf, S. Mukherjee, M. Gibson, R. Banerjee, Microstructure and wear resistance of an intermetallic-based $Al_{0.25}Ti_{0.75}$CoCrFeNi high entropy alloy. Mater. Chem. Phys. **210**, 197–206 (2018). https://doi.org/10.1016/j.matchemphys.2017.06.034
56. Y. Xing, C.J. Li, Y.K. Mu, Y.D. Jia, K.K. Song, J. Tan, G. Wang, Z.Q. Zhang, J.H. Yi, J. Eckert, Strengthening and deformation mechanism of high-strength CrMnFeCoNi high entropy alloy prepared by powder metallurgy. J. Mater. Sci. Technol. **132**, 119–131 (2023). https://doi.org/10.1016/j.jmst.2022.06.009
57. R. John, A. Karati, J. Joseph, D. Fabijanic, B.S. Murty, Microstructure and mechanical properties of a high entropy alloy with a eutectic composition AlCoCrFeNi$_{2.1}$ synthesized by mechanical alloying and spark plasma sintering. J. Alloys Compd. **835**, 155424 (2020). https://doi.org/10.1016/j.jallcom.2020.155424
58. J. Wang, B. Liu, C.T. Liu, Y. Liu, Strengthening mechanism in a high-strength carbon-containing powder metallurgical high entropy alloy. Intermetallics **102**, 58–64 (2018). https://doi.org/10.1016/j.intermet.2018.07.016
59. R. Francis, G. Byrne, Duplex stainless steels—alloys for the 21st century. Metals (2021). https://doi.org/10.3390/met11050836
60. A. Azizi, H.R. Abedi, Room temperature compressive superplasticity of low-density steel. Scr. Mater. (2022). https://doi.org/10.1016/j.scriptamat.2022.114757
61. B.H. Toby, R.B. von Dreele, GSAS-II: the genesis of a modern open-source all-purpose crystallography software package. J. Appl. Crystallogr. **46**, 544–549 (2013). https://doi.org/10.1107/S0021889813003531
62. H.M. Rietveld, A profile refinement method for nuclear and magnetic structures. J. Appl. Crystallogr. **2**, 65–71 (1969). https://doi.org/10.1107/s0021889869006558
63. Y. Shadangi, K. Chattopadhyay, V. Singh, Microstructural modification and tensile behavior of IF steel processed through surface mechanical attrition treatment. JOM **72**, 4330–4339 (2020). https://doi.org/10.1007/s11837-020-04400-4
64. N.K. Mukhopadhyay, P. Paufler, Micro- and nanoindentation techniques for mechanical characterisation of materials. Int. Mater. Rev. **51**, 209–245 (2006). https://doi.org/10.1179/174328006X102475